Document Version
Final published version

Citation (APA)
Hehenberger, S. P., Caizzone, S., Thurner, S., & Yarovoy, A. (2023). Broadband Waveguide Characterization of 3D-Printed Anisotropic Dielectric Crystals. In *Proceedings of the 2023 17th European Conference on Antennas and Propagation (EuCAP)* (pp. 1-5). (17th European Conference on Antennas and Propagation, EuCAP 2023). IEEE. https://doi.org/10.23919/EuCAP57121.2023.10133599

Broadband Waveguide Characterization of 3D-Printed Anisotropic Dielectric Crystals

Simon P. Hehenberger*‡, Stefano Caizzone*, Stefan Thurner † Alexander Yarovoy‡
*Institute for Communication and Navigation, German Aerospace Center (DLR), Wessling, Germany, simon.hehenberger@dlr.de
†Microwave and Radar Institute, German Aerospace Center (DLR), Wessling, Germany
‡Microwave Sensing, Signals and Systems, Delft University of Technology, Delft, Netherlands

***Abstract*—Additive manufactured structured dielectrics with engineered permittivity tensors are promising tools for novel microwave components and are drawing increasing attention from researchers. However, design modeling and experimental verification of anisotropic materials are challenging and have not yet been thoroughly explored in the literature. In this work, a design approach based on superimposed spatial harmonics for the design of anisotropic lattices called dielectric crystals is used. Furthermore, the plane wave expansion method (PWEM) is identified as a powerful tool for modeling the effective permittivity tensor. A wideband material characterization measurement setup based on rectangular waveguides is utilized for experimental verification. Experiments with uniaxial anisotropic dielectric crystals are carried out and are shown to be in satisfying agreement with our theoretical modeling.**

***Index Terms*—additive manufacturing, 3D-printing, structured dielectric, dielectric crystal, uniaxial anisotropy, biaxial anisotropy, anisotrop, permittivity tensor, waveguide measurement, broadband, material characterization**

I. INTRODUCTION

In the last decade, the possibilities enabled by additive manufacturing (AM) exploded, and researchers are investigating the additional degrees of freedom AM offers to design and manufacture new microwave components [1]. Due to inherent problems and the cost of incorporating metal into the additive manufacturing process, many researchers have investigated all-dielectric approaches to create high-frequency devices such as dielectric resonator antennas [2][3], lenses [4] and substrates [5]. Devices have been designed and successfully manufactured as solids and with graded-index (GRIN) approaches where different fill fractions of some base material are used to vary the effective material permittivity throughout the device spatially. Most works concerning GRIN devices deal only with isotropic material parameters. However, due to the capability of additive manufacturing to create complex 3D structures, it is possible to engineer the individual tensor components of the dielectric response. Anisotropic material printing has been successfully demonstrated in [6] and employed in [7] to engineer a dielectric resonator antenna with uniaxial anisotropic material. However, so far, only 2D periodic structures have been utilized to engineer the permittivity tensor of printed materials. In this work, we extend the concept of 3D periodic dielectric crystals introduced in [8] and investigate their potential to engineer the anisotropy of structured dielectrics. Furthermore, multiple waveguide standards are utilized to carry out a broadband characterization of said anisotropic crystals. The paper is structured as follows. Section two deals with the design of a dielectric crystal and introduces the different cases of anisotropy and how they are obtained with dielectric crystals. Section three explains the symmetry of dielectric crystals for different anisotropy cases and how to extract the permittivity tensor components from the band diagram. Section four explains the waveguide measurement setup, and section five gives insight into the sample manufacturing and measurement results. A conclusion of the presented work is given in section six.

II. ANISOTROP DIELECTRIC CRYSTALS

The method introduced in [8] takes a general approach to design the shape of dielectric unit cells, by utilizing superimposed spatial harmonics along the reciprocal lattice vectors of the desired crystal geometry. While the original work only concerned itself with the case of isotropic materials, we build on the spatial harmonic design method and investigate the possibility of creating anisotropic dielectric crystals. This is done by manipulating the amplitudes of individual spatial harmonics in order to create an anisotropic unit cell. To explain this let's consider a unit cell with simple cubic symmetry, lattice constant a, created with $N = 3$ spatial harmonics and amplitudes $A_\mathrm{i},\ i = 1 \dots\ N$ that exhibits an effective permittivity tensor

$$[\varepsilon_\mathrm{r}] = \begin{bmatrix} \varepsilon_\mathrm{a} & 0 & 0 \\ 0 & \varepsilon_\mathrm{b} & 0 \\ 0 & 0 & \varepsilon_\mathrm{c} \end{bmatrix}. \tag{1}$$

Four general cases of tensor component configurations can be identified from equation (1):

- *Isotropic* - An isotropic unit cell is generated by choosing $A_\mathrm{i} = 1\ \forall\ i = 1 \dots N$. Resulting in a unit cell depicted in Figure 1a, and obtaining a permittivity tensor with $\varepsilon_\mathrm{a} = \varepsilon_\mathrm{b} = \varepsilon_\mathrm{c}$.
- *Uniaxial anisotropic* - Uniaxial anisotropy can be created when two axis of the crystal obtain the same effective permittivity $\varepsilon_\mathrm{a} = \varepsilon_\mathrm{b} \neq \varepsilon_\mathrm{c}$. Anisotropic materials where $\varepsilon_\mathrm{a,b} > \varepsilon_\mathrm{c}$ are called negative birefringent and materials where $\varepsilon_\mathrm{a,b} < \varepsilon_\mathrm{c}$ are called positive birefringent.

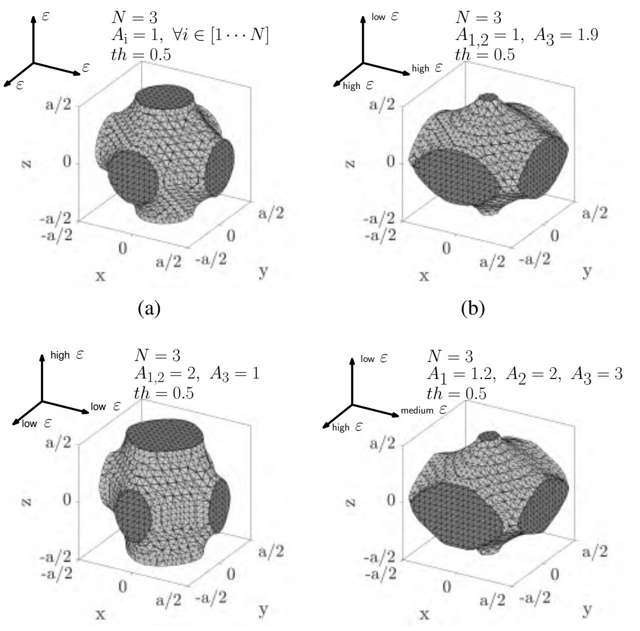

(a) (b)

(c) (d)

Fig. 1. Examples of anisotropic unit cells. (a) isotropic; (b) uniaxial anisotropic with negative birefringence; (c) uniaxial anisotropic with positive biregringence; (d) biaxial anisotropic

Uniaxial behavior can be achieved by assigning the same amplitude to two spatial harmonics that make up the crystal and a different to the third.

  - To create a crystal with *negative birefringence* we assign $A_{1,2} = 1$ and $A_3 = 1.9$, resulting in a unit cell depicted in Figure 1b.
  - In contrast to the crystal with negative birefringence, we assign $A_{1,2} = 2$ and $A_3 = 1$, resulting in a unit cell with *positive birefringence* as depicted in Figure 1c.

- *Biaxial anisotropic* - An biaxial anisotropic unit cell is generated by choosing $A_1 = 1.2,\ A_2 = 2,\ A_3 = 3$. Resulting in a unit cell as depicted in Figure 1d, and obtaining a permittivity tensor with $\varepsilon_a \neq \varepsilon_b \neq \varepsilon_c$.

The material can be created by additive manufacturing a lattice of the unit cells with a fused deposition modeling process (FDM) utilizing a filament with stock relative permittivity $\varepsilon_{\mathrm{r,bulk}}$. Different values for the individual effective permittivity tensor components in equation (1) can be obtained by employing materials with different $\varepsilon_{\mathrm{r,bulk}}$ or by playing around with the spatial harmonic amplitudes A_{i}.

III. SIMULATION OF ANISOTROP DIELECTRIC CRYSTALS

Most works dealing with additive-manufactured GRIN devices use effective media theories (EMT) to model the effective relative permittivity of the employed unit cell. However, EMTs usually assume isotropy of the resulting composite and are, therefore, ill-suited to predict anisotropic material parameters. In [7], a Floquet port method is employed to simulate the reflection and transmission of a 2D infinite slab and extract the effective material parameters via the Nicholson-Ross-Weir (NRW) method [9][10]. This work again takes a more general approach by computing the propagating modes in the infinite 3D lattice and computing the effective material parameters for small-magnitude wave vectors from the dispersion of the crystal. Frequencies of propagating modes in the crystal can be found by solving the eigenvalue problem

$$\nabla \times \frac{1}{\varepsilon(\vec{r})} \times \vec{H}(\vec{r}) = \left(\frac{\omega}{c_0}\right)^2 \vec{H}(\vec{r}) \tag{2}$$

as obtained from Maxwell's equation, where $\vec{H}(\vec{r})$ is the magnetic field (eigenvector) and $\left(\frac{\omega}{c_0}\right)^2$ represents the eigenvalue of the propagating mode, where c_0 represents the speed of light, and ω the mode frequency. Here we utilize the plane wave expansion method (PWEM) to solve equation (2) for the mode frequencies of a given Bloch-wave vector β. Doing this for a set of wave vectors along the boundary of the irreducible Brillouin zone (IBZ) and plotting the resulting eigenfrequencies against the wave vector gives the band diagram of the geometry. From the band diagram, the effective refractive index n_{eff} of the material can be extracted for low-magnitude Bloch-wave vectors with

$$n_{\mathrm{eff}} = \frac{\left|\vec{\beta}\right|}{k_0} = \sqrt{\varepsilon_{\mathrm{r,eff}}\mu_{\mathrm{r}}} \tag{3}$$

which for non-magnetic materials ($\mu_{\mathrm{r}} = 1$) is equal to the square root of the effective relative permittivity $\varepsilon_{\mathrm{r,eff}}$. Evaluating this relationship for different directions of the Bloch-wave vector $\vec{\beta}$ can give insight into the anisotropic behavior of the crystal. The PWEM is usually evaluated for Bloch vectors around the irreducible Brillouin zone of the unitcell. The IBZ depends on the symmetry of the unitcell and the relevant symmetries for this work are discussed below.

A. Crystal Symmetries

For the isotropic case, as depicted in Figure 1a), the crystal obtains a simple cubic symmetry for which the corresponding IBZ is depicted in Figure 2a. For the anisotropic case, no simple cubic symmetry can be assumed. Although the dimensions of the unit cell ($a \times a \times a$) stay the same as in the isotropic case, for the anisotropic unit cells depicted in Figures 1c, 1b and 1d respectively, the internal symmetry is not the same in all axis. A primitive tetragonal and orthorhombic crystal symmetry have to be considered for uniaxial and biaxial anisotropic cases for which the IBZ is depicted in Figures 2b and 2c respectively. A more detailed account of crystal symmetries and their corresponding Brillouin zones and key points of symmetry can be found in [11].

B. Effective Material Parameter Extraction

The PWEM results for the isotropic crystal, as depicted in Figure 1a, evaluated around the IBZ as sketched in Figure 2a is shown in Figure 3 together with the extracted effective permittivity according to equation (3). The two polarizations of the fundamental mode are depicted in orange and blue

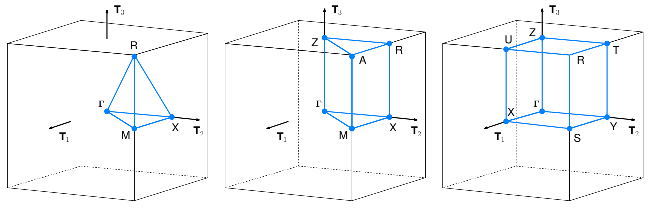

(a) (b) (c)

Fig. 2. Brillouin zones of an (a) isotropic, (b) uniaxial anisotropic, (c) biaxial anisotropic unit cell with key points of symmetry.

while the area in which a linear dispersion approximation is satisfied with an error of up to 1% is shaded in green. One is able to observe linear dispersion with equal slopes for all propagation directions up to a normalized frequency of $\omega = 0.0254$, confirming the expected isotropic nature of the crystal. The extracted effective relative permittivity is blank in the Γ-point because the magnitude of the Bloch vector is defined to be 0 at Γ, leading to an obviously wrong result with equation (3). Effective permittivity values at higher order magnitude Bloch vectors do not make sense because equation (3) relies on the assumption of linear dispersion, which breaks down above a certain frequency threshold. Similar plots of the band diagram and extracted effective permittivity for the uniaxial and biaxial anisotropic cases, with IBZs shown in Figures 2b and2c, are provided in Figures 4 and 5, respectively. For the uniaxial case, one is able to observe in Figure 4 that the orthogonal polarizations in the fundamental mode obtain different slopes in the band diagram for the Bloch vectors along the path $\Gamma - \mathrm{X}$ (corresponding to a propagation direction along $\hat{x}$ or $\hat{y}$), which is not the case for the Bloch vector path $\Gamma - \mathrm{Z}$ (corresponding to a propagation direction along $\hat{z}$). The same conclusion can be drawn from the extracted relative permittivity, although the effect is more visible in the plot of the permittivity. From the band diagram and extracted relative permittivities of the biaxial case in Figure 5, one can see that the orthogonal polarizations in the fundemental mode experience different effective material parameters for the three Bloch vector paths $\Gamma - \mathrm{X}$, $\Gamma - \mathrm{Y}$ and $\Gamma - \mathrm{Z}$, confirming the biaxial anisotropic behvaior of the dielectric crystal.

IV. MEASUREMENT SETUP

In general, the measurement of dielectric material parameters prove to be quite difficult. The field encompasses a large number of measurement techniques and material types. There are several trade-offs to consider when selecting a measurement approach, and an excellent and extensive overview of the topic is given in [12]. Out of the many measurement options available, the resonance method is usually preferred due to its capability to precisely measure the loss tangent of low-loss materials [13] and has been successfully employed to characterize 3D-printed graded materials in [8]. However, resonance methods are not capable of extracting the individual permittivity tensor components from the material under test (MUT). Furthermore, resonance measurement systems are only capable of characterizing the MUT at a single frequency point. To circumvent the shortcomings of a resonance approach, a rectangular waveguide measurement system, as depicted in Figure 6, is employed in this work to measure the permittivity tensor components across a wide frequency range. The measurement is performed by inserting a MUT sample into a waveguide structure and recording transmission and reflection coefficients via a Vector Network Analyzer (VNA). The effective material parameters are computed in postprocessing via the Nicholson-Ross-Weir (NRW) method. Although the NRW method can

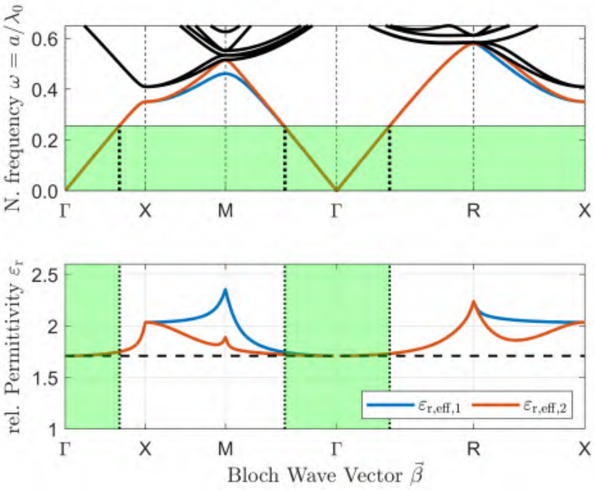

Fig. 3. Top: band diagram of an isotropic dielectric crystal with simple cubic symmetry. Bottom: extracted effective refractive index for the two orthogonal polarization of the fundamental mode assuming linear dispersion. The modes relating to the orthogonal polarizations in the fundamental mode are displayed in color. Areas where linear dispersion applies are shaded in green.

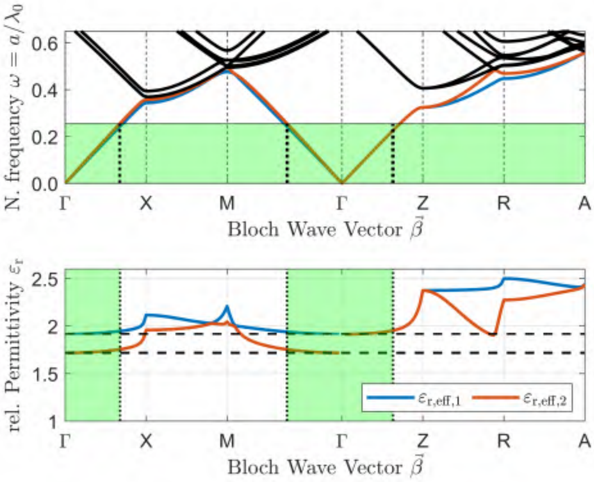

Fig. 4. Top: band diagram of an uniaxial anisotrop dielectric crystal with primitive tetragonal symmetry. Bottom: extracted effective refractive index for the two orthogonal polarization of the fundamental mode assuming linear dispersion. The modes relating to the orthogonal polarizations in the fundamental mode are displayed in color. Areas where linear dispersion applies are shaded in green.

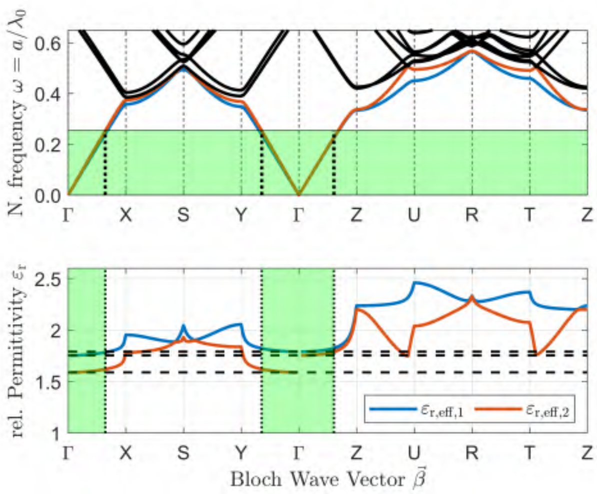

Fig. 5. Top: band diagram of an biaxial anisotropic dielectric crystal with orthorhombic symmetry. The modes relating to the orthogonal polarizations in the fundamental mode are displayed in color. Bottom: extracted effective refractive index for the two orthogonal polarization of the fundamental mode assuming linear dispersion. The modes relating to the orthogonal polarizations in the fundamental mode are displayed in color. Areas where linear dispersion applies are shaded in green.

TABLE I
RECTANGULAR WAVEGUIDE STANDARDS UTILIZED IN THIS WORK FOR EFFECTIVE PERMITTIVITY MEASURMENT OF ADDITIVE MANUFACTURED DIELECTRIC CRYSTALS.

WG	Frequency [GHz]	Width [mm]	Height [mm]
WR284	2.60 - 3.95	72.14	36.09
WR187	3.95 - 5.85	47.50	23.75
WR137	5.85 - 8.20	34.79	17.40
WR90	8.20 - 12.40	22.86	10.16

extract both complex permittivity and permeability of a MUT, the extraction of both complex quantities causes ill-behavior of the procedure at frequencies corresponding to one-half wavelength in the sample [14]. As this work only deals with dielectric materials, the assumption $\mu_r = 1$ is generally imposed on the utilized NRW procedure. This leads to a more accurate and stable computation of the MUTs complex permittivity [14]. By doing this for the same MUT in the crystal's three different principal orientations, the permittivity tensor's individual components can be extracted. Accurately machining the samples to fit the waveguide dimensions is essential since gaps between the sample and waveguide walls can cause significant errors in the extracted material parameters [15]. Although traveling-guided wave setups are considered broadband, they are usually only employed in the fundamental mode of the utilized waveguide. Therefore, this work uses several consecutive rectangular waveguide standards to cover a wide frequency range, as listed in Table I. The system is calibrated with a through-reflect-line approach for every waveguide standard before measurement.

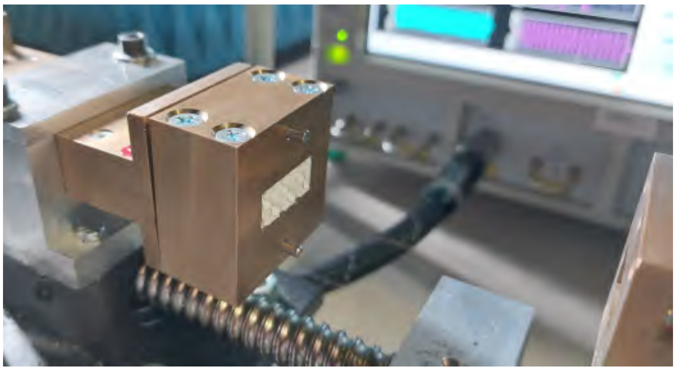

Fig. 6. Rectangular waveguide measurement setup for effective permittivity measurement.

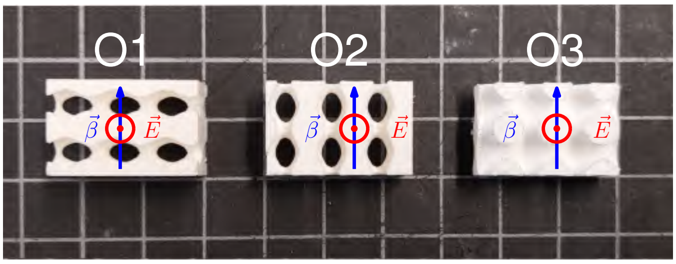

Fig. 7. Additive manufactured samples of the same uniaxial anisotrop dielectric crystal in three different orientations for material characterization measurements in a WR90 rectangular waveguide including annotation indicating the direction of propagation in the waveguide $\vec{\beta}$ in blue and polarization of the electric field $\vec{E}$ in red.

V. MANUFACTURING AND MEASUREMENT RESULTS

First experiments are carried out with an uniaxial anisotropic lattice with negative birefringence. Manufacturing is done with an Ultimaker 3 FDM additive manufacturing machine using the Ultimaker white polylactic (PLA) filament. The Ultimaker PLA was also used in [8] and measured to have a bulk relative permittivity of $\varepsilon_{\mathrm{r,bulk}} = 2.66$ and loss tangent $\tan\delta = 0.062$. Three samples with spatial harmonic amplitudes $A_{1,2} = 1$, $A_3 = 2$, a lattice constant of $a = 7.5$ mm, and threshold $th = 0.45$ have been printed with different orientations for anisotropic characterization. The initial samples have been printed in the dimensions of the WR284 waveguide standard and two unit cells thick. Samples for the consecutively smaller waveguide standard as listed in Table I were cut out from the original sample to reduce errors produced over mulitple print-jobs. The samples for all orientaitions in their shape for the last mesurement (dimensions of the WR90 waveguide) are depicted in Figure 7. The complex permittivity, extracted from the S-parameter measurements with the MUT in the rectangular waveguide system, is plotted as a function of frequency for all measured orientations and waveguide standards in Figure 8 together with the extracted permittivity values from the PWEM simulations.

An excellent agreement between the effective permittivity extracted from PWEM simulations and measurements for

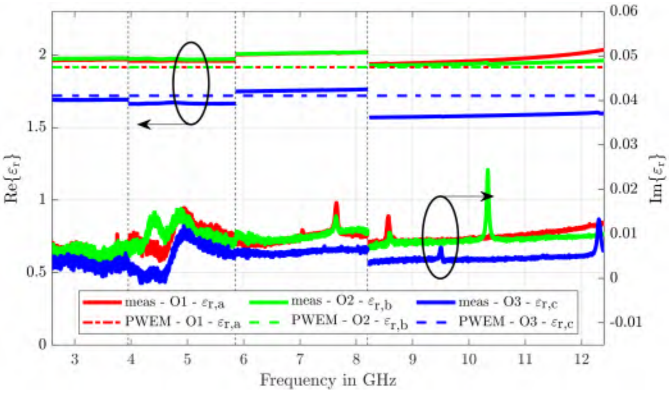

Fig. 8. Effective permittivity results extracted from S-parameter measurements of three different samples correspondig to different orientations of the same anisotrop dielectric crystal. Measurments were performed with the rectangular waveguide standards WR284, WR187, WR137 and WR90.

all three orientations is observed for all utilized waveguide standards. Differences in the extracted effective permittivity values between different waveguide standards are most likely caused by small air gaps between the sample and the waveguide wall. The effect of the gaps gets more severe with increasing frequency, as the samples get smaller but machining tolerances stay the same. This effect is especially apparent for the measurement of the sample O3 which exhibits free-standing protruding features, as depicted in Figure 7, touching the upper waveguide wall that were difficult to machine equally, hence showing the largest measurement error. Nevertheless, the measurements confirm that the dielectric crystal behaves effectively as a uniaxial anisotropic material.

VI. CONCLUSION

The design of anisotropic dielectric crystals with superimposed spatial harmonics is discussed for uniaxial with both positive and negative birefringence and biaxial cases. The changes in crystal symmetry due to the anisotropy of the crystal have been explained, and simulations via the plane wave expansion method have been carried out to extract the effective permittivity tensor for large wavelengths. An additive manufacturing technique is employed to 3D print a uniaxial anisotropic crystal in three different orientations. Individual samples have been subjected to material characterization measurements with a rectangular waveguide measurement system in multiple sizes. The measurement results show an excellent agreement with simulation data and confirm the applicability of the spatial harmonics design approach and PWEM simulation to the design of anisotropic dielectric crystals. Minor measurement deviations can be observed in different waveguide standards, which can be attributed to machining tolerances.

REFERENCES

[1] E. S. Rosker, R. Sandhu, J. Hester, M. S. Goorsky, and J. Tice, ‘Printable materials for the realization of high performance RF components: Challenges and opportunities’, Int. J. Antennas Propag., vol. 2018, pp. 1–19, 2018, DOI: 10.1155/2018/9359528

[2] A. A. Althuwayb et al., ‘3-D-printed dielectric resonator antenna arrays based on standing-wave feeding approach’, IEEE Antennas Wirel. Propag. Lett., vol. 18, no. 10, pp. 2180–2183, Oct. 2019, DOI: 10.1109/LAWP.2019.2939734.

[3] Z.-X. Xia, K. W. Leung, and K. Lu, ‘3-D-printed wideband multi-ring dielectric resonator antenna’, IEEE Antennas Wirel. Propag. Lett., vol. 18, no. 10, pp. 2110–2114, Oct. 2019, NOI: 10.1109/LAWP.2019.2938009.

[4] B. P. Soh, W. M. Lee, P. L. Kench, W. M. Reed, M. F. McEntee, and P. C. Brennan, ‘Test set readings predict clinical performance to a limited extent: preliminary findings’, in Medical Imaging 2013: Image Perception, Observer Performance, and Technology Assessment, Lake Buena Vista (Orlando Area), Florida, USA, 2013, DOI: 10.1117/12.2000708

[5] S. Zhang, C. C. Njoku, W. G. Whittow, and J. C. Vardaxoglou, ‘Novel 3D printed synthetic dielectric substrates’, Microw. Opt. Technol. Lett., vol. 57, no. 10, pp. 2344–2346, Oct. 2015, DOI: 10.1002/mop.29324

[6] C. R. Garcia et al., ‘3d printing of anisotropic metamaterials’, Prog. Electromagn. Res. Lett., vol. 34, pp. 75–82, 2012, DOI: 10.2528/PIERL12070311

[7] C. D. Morales, C. Morlaas, A. Chabory, R. Pascaud, M. Grzeskowiak, and G. Mazingue, ‘Single-fed circularly polarized dielectric resonator antenna using a uniaxial anisotropic material’, in Antennas and Propagation Conference 2019 (APC-2019), Birmingham, UK, 2019, DOI: 10.1049/cp.2019.0713

[8] S. P. Hehenberger, A. P. T. Adithyababu, and S. Caizzone, ‘Effective permittivity measurement of 3D-printed dielectric crystals’, in 2022 16th European Conference on Antennas and Propagation (EuCAP), Madrid, Spain, 2022, DOI: 10.23919/EuCAP53622.2022.9769370.

[9] A. M. Nicolson and G. F. Ross, ‘Measurement of the intrinsic properties of materials by time-domain techniques’, IEEE Trans. Instrum. Meas., vol. 19, no. 4, pp. 377–382, Nov. 1970, DOI: 10.1109/TIM.1970.4313932.

[10] W. B. Weir, ‘Automatic measurement of complex dielectric constant and permeability at microwave frequencies’, Proc. IEEE Inst. Electr. Electron. Eng., vol. 62, no. 1, pp. 33–36, 1974, DOI: 10.1109/PROC.1974.9382.

[11] W. Setyawan and S. Curtarolo, ‘High-throughput electronic band structure calculations: Challenges and tools’, Comput. Mater. Sci., vol. 49, no. 2, pp. 299–312, Aug. 2010, DOI: 10.1016/j.commatsci.2010.05.010.

[12] Clarke, R. N., Andrew P. Gregory, David S. Cannell, Maria L. Patrick, S J Wylie, Ian J. Youngs and G J Hill. “A guide to the characterisation of dielectric materials at RF and microwave frequencies.” (2003).

[13] A. K. Jha and M. J. Akhtar, ‘A generalized rectangular cavity approach for determination of complex permittivity of materials’, IEEE Trans. Instrum. Meas., vol. 63, no. 11, pp. 2632–2641, Nov. 2014, DOI: 10.1109/TIM.2014.2313415.

[14] J. Baker-Jarvis, E. J. Vanzura, and W. A. Kissick, ‘Improved technique for determining complex permittivity with the transmission/reflection method’, IEEE Trans. Microw. Theory Tech., vol. 38, no. 8, pp. 1096–1103, Aug. 1990, DOI: 10.1109/22.57336.

[15] S. B. Wilson, ‘Modal analysis of the “gap effect” in waveguide dielectric measurements’, IEEE Trans. Microw. Theory Tech., vol. 36, no. 4, pp. 752–756, Apr. 1988, DOI: 10.1109/22.3581.